Advancing laser ablation assessment in hyperspectral imaging through machine learning

Viacheslav V. Danilov [a,*], Martina De Landro [a], Eric Felli [b], Manuel Barberio [c], Michele Diana [d,e], Paola Saccomandi [a,*]

[a] *Department of Mechanical Engineering, Politecnico di Milano, Milan, Italy*
[b] *Department of Visceral Surgery and Medicine, Inselspital, Bern University Hospital, University of Bern, Switzerland*
[c] *Department of General Surgery, Cardinal G. Panico Hospital, Tricase, Italy*
[d] *Research Institute against Digestive Cancer, Strasbourg, France*
[e] *ICube Laboratory, University of Strasbourg, Strasbourg, France*

A B S T R A C T

Hyperspectral imaging (HSI) is gaining increasing relevance in medicine, with an innovative application being the intraoperative assessment of the outcome of laser ablation treatment used for minimally invasive tumor removal. However, the high dimensionality and complexity of HSI data create a need for end-to-end image processing workflows specifically tailored to handle these data. This study addresses this challenge by proposing a multi-stage workflow for the analysis of hyperspectral data and allows investigating the performance of different components and modalities for ablation detection and segmentation. To address dimensionality reduction, we integrated principal component analysis (PCA) and t-distributed stochastic neighbor embedding (t-SNE) to capture dominant variations and reveal intricate structures, respectively. Additionally, we employed the Faster Region-based Convolutional Neural Network (Faster R–CNN) to accurately localize ablation areas. The two-stage detection process of Faster R–CNN, along with the choice of dimensionality reduction technique and data modality, significantly influenced the performance in detecting ablation areas. The evaluation of the ablation detection on an independent test set demonstrated a mean average precision of approximately 0.74, which validates the generalization ability of the models. In the segmentation component, the Mean Shift algorithm showed high quality segmentation without manual cluster definition. Our results prove that the integration of PCA, t-SNE, and Faster R–CNN enables improved interpretation of hyperspectral data, leading to the development of reliable ablation detection and segmentation systems.

1. Introduction

Hyperspectral imaging (HSI), a rapidly advancing technique for collecting and processing spectral data from objects or scenes, has become a crucial tool in diverse applications such as remote sensing, agriculture, food industry, mineral exploration, and biomedicine. In the biomedical context, HSI holds great promise for applications such as detecting and identifying diseased tissue, monitoring disease progression, and assessing treatment effectiveness. Unlike traditional optical imaging, HSI is unique in its ability to capture rich spectral information, enabling material identification, classification, and quantification.

Recently, HSI has been innovatively applied to assess thermal damage induced by laser-mediated thermal treatment, showing promising results. In this minimally invasive therapy, laser light is delivered through a fiber optic to induce local necrosis in malignant cells. The goal of laser ablation treatment is the absence of pathologic residual tissue, which also depends on accurate control of the ablative margin around the tumor perimeter [1]. To this end, having a reliable approach for assessing the thermal effect induced in the organ under treatment is crucial. Current solutions involve image and sensor-based temperature measurements [2–4] and the estimation of tissue thermal damage using simplified models that rely on temperature and treatment time. Limitations of both the thermal damage model and thermometry techniques, such as simplifying model assumptions and potential temperature measurement errors in the specific context, can introduce a degree of uncertainty into the ablated margins and, consequently, the

---

determination of the treatment effect.

Thus, several groups have recently started investigating the use of alternative approaches for the direct estimation of thermal effects, independent of the prior measurement of the tissue temperature evolving during thermal ablation [5,6]. In particular, optical techniques can effectively discriminate between normal and thermally damaged tissue, as tissue chromophores undergo changes based on the thermal state of the tissue [7,8]. Among the optical approaches, HSI has proven to be a valid solution for assessing the thermal state of tissue in the ablative therapy field [6,9,10]. Indeed, HSI can detect the spectral variation of relevant temperature-dependent tissue chromophores, such as deoxyhemoglobin, methemoglobin, lipids, and water. Extraction of valuable information from HSI data and image segmentation are two mandatory steps to use HSI technology for the mentioned purpose.

In this study, we propose a workflow for processing and analyzing hyperspectral images obtained during laser-mediated thermal treatment of living tissue, specifically targeting organs such as the liver, pancreas, and stomach. The goal is to evaluate various algorithms and processing modalities for thermal ablation detection and segmentation, utilizing the spectral features provided by HSI [10]. Indeed, several challenges hinder the widespread adoption of HSI for this purpose and for biomedical imaging in general. These include the need for standardization of data acquisition and processing methods to ensure reproducibility and comparability of results across studies [11]. In addition, the high volume of data generated, coupled with the complexity of HSI systems, presents barriers to the rapid adoption of this technology in clinical settings [12,13]. The primary challenges are related to the high dimensionality and complexity of the HSI data, which require efficient and robust methods for processing, analysis, visualization, and interpretation. In addition, HSI faces technical limitations such as low spatial resolution, long acquisition time, high cost, and limited availability of suitable light sources and detectors [14]. As a result, the current research landscape in medical HSI focuses on the application of dimensionality reduction, detection, and clustering techniques. Some of the latest advancements include the development of novel dimensionality reduction algorithms, such as nonlinear diffusion and tensor-based analysis, which are used to simplify the dimension of hyperspectral data while maintaining data information [15,16]. These techniques help reduce redundant spectral information in hyperspectral images, enabling more efficient analysis and interpretation of the data. Detection involves identifying specific features or patterns in hyperspectral data, which is useful for various medical applications such as disease diagnosis and classification [17]. Clustering, as an unsupervised machine learning technique, is used to group similar data points together, helping to discover patterns and relationships in the data [18,19]. Furthermore, to enhance the accuracy and efficiency of HSI analysis, the development of more advanced machine learning techniques, such as deep learning algorithms, is crucial for feature extraction and classification [13,17, 20].

In our work, we focus on overcoming these challenges and advancing the application of dimensionality reduction, detection, and clustering in HSI, specifically in the context of tissue ablation assessment. Our study evaluates the performance of different modalities for ablation detection and segmentation in hyperspectral images, focusing on the evaluation of thermal effects induced by laser ablation treatment in an *in vivo* animal model. Our study evaluates the performance of different modalities for ablation detection and segmentation in hyperspectral images, focusing on the evaluation of thermal effects induced by laser ablation treatment in an *in vivo* animal model. Additionally, the Faster Region-based Convolutional Neural Network (Faster R–CNN) was used to identify ablated regions. The results of our study are expected to contribute to the integration of HSI technology into clinical practice, ultimately benefiting various medical applications.

2. Materials and methods

2.1. Experimental strategy

The experimental study was conducted during laser ablation procedures on live pigs. The objective of the research was to utilize HSI to detect thermal damage induced in vital organs such as the liver, pancreas, and stomach during the treatment. The selection of the animal model was motivated by the necessity of reproducing a preclinical scenario as closely as possible to a potential application in clinical settings, thus presenting similar technical challenges.

The experiments were performed at the Institute for Image Guided Surgery in Strasbourg, France. This experimental study was approved by the local Ethical Committee on Animal Experimentation (ICOMETH No. 38.2015.01.069) and by the French Ministry of Higher Education and Research (protocol N°APAFiS-19543-2019030112087889, approved on March 14, 2019). All animals were treated in accordance with the ARRIVE guidelines, the French legislation on the use and care of animals, and the guidelines of the Council of the European Union (2010/63/EU).

Each animal underwent treatment in the three organs: liver, pancreas, or stomach. A total of 3 adult Sus scrofa domesticus with a mean weight of 33.5 ± 4.9 kg were housed in an enriched environment with constant humidity and temperature for 48 h. A circadian light-dark cycle was maintained throughout the study. Prior to surgery, all animals were fasted for 24 h with ad libitum access to water. Thirty minutes before surgery, they were sedated with zolazepam and tiletamine at a dose of 10 mg/kg. Anesthesia was induced with propofol administered via an 18-gauge intravenous catheter in the ear vein, with a dosage of 3 mg/kg. Anesthesia was maintained with rocuronium (0.8 mg/kg) and isoflurane (2 %). Vital signs were monitored using a standard respiratory machine, Primus (Dräger, Lübeck, Germany). At the end of the procedure, animals were euthanized with a lethal dose of pentobarbital (40 mg/kg) under 5 % isoflurane anesthesia.

Contactless laser ablation was performed in a laparotomy configuration on several defined areas of the liver, pancreas, and stomach surfaces using a LuOcean Mini 4 diode laser (*Lumics*, Berlin, Germany) that delivered radiation to a 400-μm fiber applicator. A collimator was placed at the tip of the applicator to direct an 808-nm laser beam onto the tissue surface. The collimated beam was approximately 1.5 cm in diameter. The laser current was typically set between 3000 and 3500 mA, corresponding to a laser power range of approximately 3–6 W. The tissue was irradiated until specific temperature thresholds were reached (i.e., 60, 70, 80, 90, 100 and 110 °C), as shown in Fig. 1. Temperature monitoring was performed using a FLIR T540 thermal camera (*Teledyne FLIR*, Wilsonville, USA). These temperature thresholds were used as
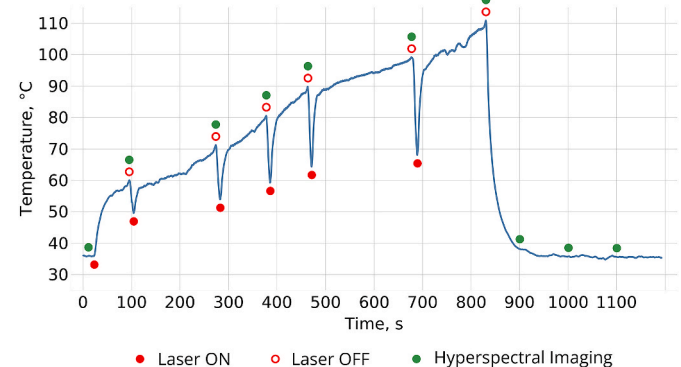

Fig. 1. Temperature profile during laser ablation experiments on porcine organs, showcasing the dynamic temperature changes over time. Each time step corresponds to a different data acquisition, with temperature thresholds serving as indicators of the thermal effects produced.

indicators of the thermal effect produced. Once the set temperature threshold was reached, the laser system was turned off and a TIVITA hyperspectral camera (*Diaspective Vision GmbH*, Am Salzhaff, Germany) acquired the data. Hypercubes of 100 wavelength bands each were collected by the hyperspectral camera for each acquisition step.

2.2. Hyperspectral data acquisition

During our experimental study, we used a commercial TIVITA hyperspectral camera to acquire hypercubes of size 640 × 480 × 100 voxels, indicating 640 × 480 pixels for 100 bands, and regular RGB images at each acquisition step. These bands were acquired directly from the hyperspectral camera without additional pre-processing. The hypercube was acquired in approximately 6 s and synchronized with the absence of breathing motion using a protocol implemented for animal anesthesia. Polyurethane markers were placed around the target area to serve as references for superimposing the hyperspectral images, which were acquired using target areas selected according to the hyperspectral camera manufacturer's guidelines.

The hyperspectral camera was positioned vertically at a distance of 40 cm from the surgical field [21] to minimize extraneous light on the measurement area. In addition, all light sources in the operating room were turned off during HSI acquisition, except for the camera lights. The acquisition of a single hypercube is performed using a camera-specific module of the Perception Studio software (*Perception Park GmbH*, Graz, Austria). The spectral range of the camera is 500–995 nm. To ensure intense, broadband, temperature-stable, homogeneous, and fast pulse radiation, we used a 20 W Halogen lamp (Osram Halospot 70) as the light source. The calibration of the wavelength is performed during camera production. Furthermore, dark current effects are corrected by the developed software component after the hypercube acquisition.

The camera collects and processes information from the electromagnetic spectrum to measure the reflectance spectra produced by the target. To convert image data from radiance to relative reflectance, we used a white reference object characterized by high diffuse reflectance to create a reference hypercube before starting the measurements.

We employed two different imaging modes to capture hyperspectral information, where these modes constitute the data modalities. Specifically, the hyperspectral data used in this study were collected using a reflectance-based (Ref) HSI technique, which measures the amount of light reflected by the sample at different wavelengths, thus providing information about the surface properties and morphology of the sample. From reflectance-based HSI, it is also possible to obtain absorbance-based (Abs) images [22]. Absorbance-based HSI measures the absorption of light by the sample at different wavelengths, providing information about the chemical composition and concentration of the sample. The combination of these two HSI modes provides a more comprehensive understanding of the sample properties and facilitates accurate and informative analysis. Both absorbance and reflectance data modalities were considered in the analysis.

As part of our investigation, we included hyperspectral cubes from 20 experiments conducted under identical conditions in our study. The hyperspectral cubes were collected in three distinct stages. In the first stage, the cubes were collected prior to laparotomy at the basal body temperature of 37 °C. In the second stage, we obtained the cubes as the temperature gradually increased from 60 °C to 110 °C at 10 °C intervals. Finally, in the last stage, the cubes were collected after turning off the laser during the post-ablation phase. Thus, we obtained a total of 233 hyperspectral cubes, each consisting of 100 wavelengths, resulting in a dataset of 23,300 two-dimensional images. The temperature changes were recorded, and Fig. 1 illustrates the corresponding profile, highlighting the specific time intervals during which the hyperspectral camera and laser were activated and deactivated. Following laparotomy (the leftmost green dot in Fig. 1), the tissue underwent laser irradiation until specific temperature thresholds were reached. Throughout this process, the temperature was continuously monitored using a FLIR T540

thermal camera. Subsequently, the laser system was turned off, and the TIVITA hyperspectral camera acquired hyperspectral data. The graph shows the temperature change over time, with each time step representing a different data acquisition. These temperature thresholds serve as indicators of the thermal effect produced. For a visual representation of the collected data, several examples of images taken from different organs are included in Fig. 2.

2.3. Hyperspectral image analysis workflow

The workflow proposed in this study, presented in Fig. 3, consists of several key steps to extract valuable information from hyperspectral data in the laser ablation scenario. First, dimensionality reduction (detailed in *Step I: Dimensionality reduction*) is applied to reduce the high-dimensional data to a manageable size. Next, a supervised learning technique (detailed in *Step II: Detection of the ablation area*) based on neural networks is used to detect the ablation area, i.e., the region of the image where tissue has been treated by laser irradiation. Finally, an unsupervised learning technique (detailed in *Step III: Segmentation of the ablation area*) based on clustering is used to segment the spectral signature of the ablation area, allowing the identification of specific tissue types or classes of thermal damage. The proposed workflow provides a comprehensive approach to the analysis of hyperspectral data and has the potential to improve the accuracy and efficiency of diseased tissue analysis in the thermal treatment scenario.

2.3.1. Step I: dimensionality reduction

HSI captures the reflectance spectra of a scene across hundreds of narrow spectral bands, resulting in a three-dimensional data cube with two spatial dimensions and one spectral dimension. This leads to challenges such as high data volume, redundancy, noise, and complexity. To address these challenges, we employ dimensionality reduction, which aims to reduce the number of variables in the dataset (in our case, the wavelength dimension) while preserving the most relevant information. Typically, PCA and t-SNE are two different approaches used for dimensionality reduction.

PCA is a linear dimensionality reduction technique that aims to capture the global patterns and relationships in the data. It achieves this by identifying the directions (principal components) along which the data varies the most. These components are ordered so that the first few retain most of the variability present in the original data. In the context of HSI, PCA can be used for a variety of purposes, including feature extraction, data visualization, and noise reduction. It is particularly useful for identifying the main sources of variation and providing a global view of the data in a lower dimensional space. The main advantages of PCA are: (a) simplicity and ease of implementation, (b) ability to handle large datasets, and (c) preservation of the main trends and patterns in the data [23].

t-SNE is a nonlinear dimensionality reduction technique that focuses on preserving the local relationships and clusters within the data. It accomplishes this by mapping the high-dimensional data to a lower-dimensional space in a way that preserves the similarities between data points. In the context of HSI, t-SNE is particularly effective at visualizing complex patterns, clusters, and local relationships, making it a valuable tool for exploratory data analysis and pattern recognition. The key advantages of t-SNE are: (a) better visualization and clustering of data, (b) preservation of nonlinear relationships and local structures, and (c) ability to handle high-dimensional data [24].

While PCA is suitable for capturing global patterns and providing a broad overview of the data, t-SNE excels at revealing local structures and intricate relationships within the data. Both techniques have their own set of advantages and have been applied in various scenarios, including ink analysis [25,26], conservation science [27], and crop variety identification [28,29]. However, both methods have some limitations and challenges in processing HSI data. For example, PCA may not be able to capture the spectral variability and heterogeneity of HSI data, while
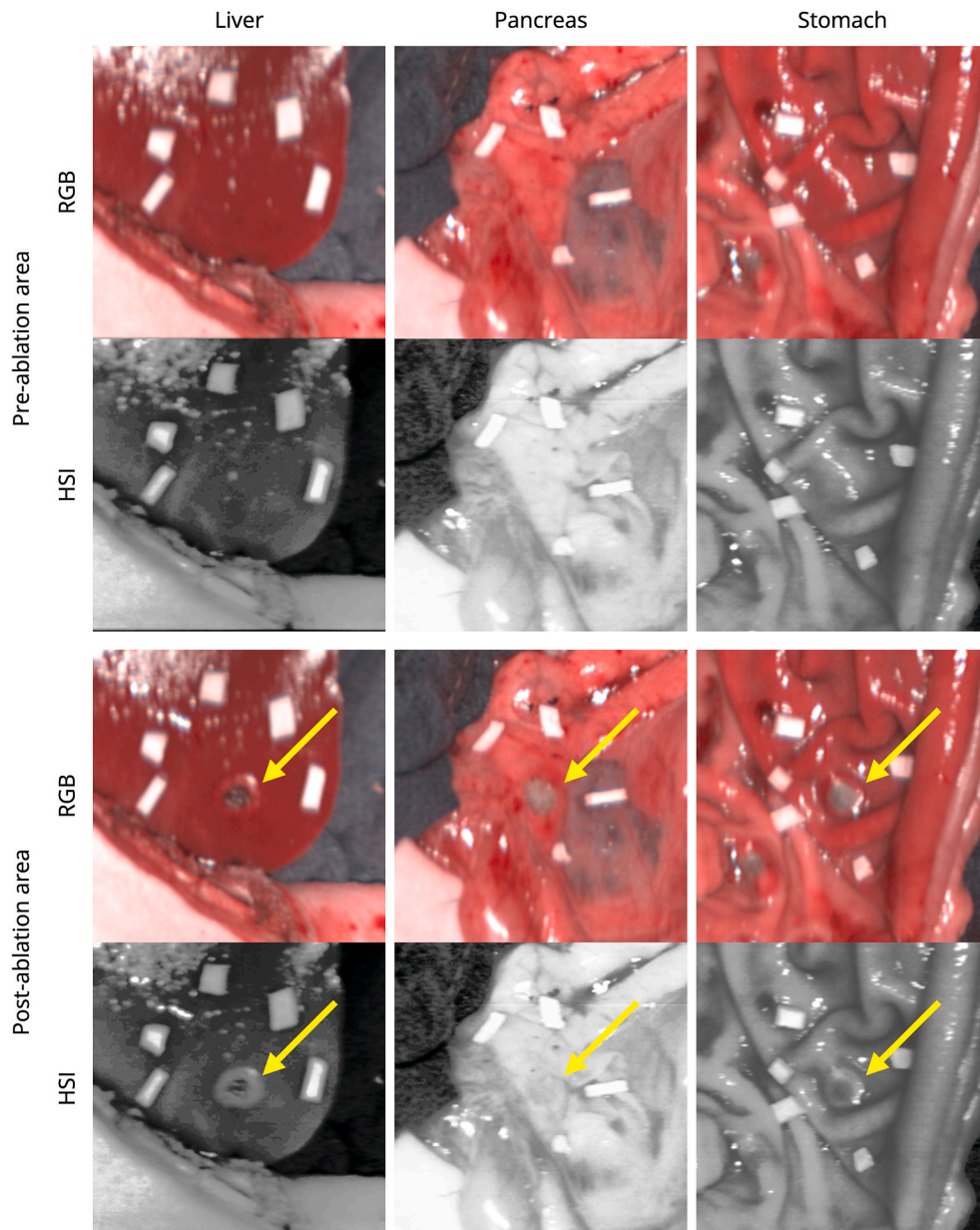
Fig. 2. Examples of ablation areas before and after laser treatment in porcine liver, pancreas and stomach. The top row represents the source RGB images, while the bottom row (grayscale images) represents reflectance images of a hyperspectral cube taken at a wavelength of 750 nm.
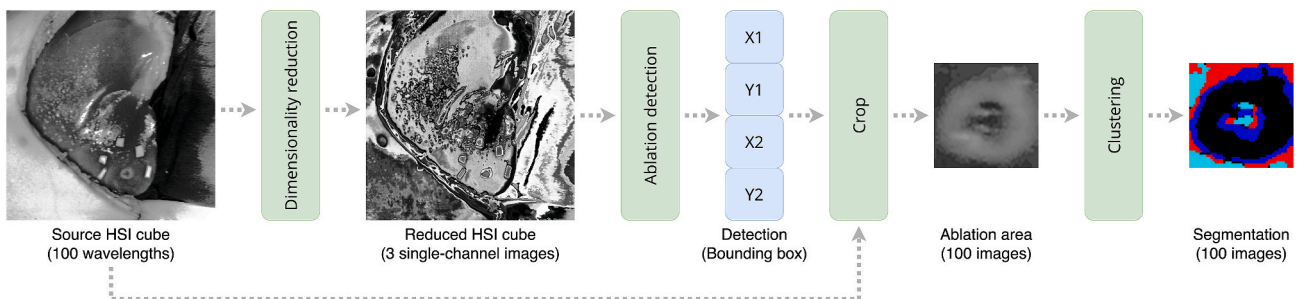

Fig. 3. Proposed workflow for hyperspectral image processing and analysis. The workflow consists of three main components: dimensionality reduction, ablation area detection using supervised learning, and spectral signature segmentation based on unsupervised learning.

t-SNE may be sensitive to the choice of parameters and initial conditions. In addition, both methods may lose some information during the dimensionality reduction process, which may affect subsequent analysis or classification tasks.

Most surfaces exhibit smooth, wavelength-dependent reflectance properties. In our dataset, we measured 100 spectral bands packed within the visible and near-infrared ranges. As a result of the data acquisition, we expect strong correlations between bands that are close in wavelength. To verify this, we analyzed the redundancy in the data using PCA decomposition, as shown in Fig. 4.

Nearly all the variance in the collected dataset is explained by the first three principal components, and altering the organs does not significantly impact the variance distribution. On average, these components explain 98.3 % of the data, with the first component explaining 84.3 %, the second explaining 10.5 %, and the third explaining 3.5 %. The remaining 7 components (from 4th to 10th) explain a total of 1 % of the data variance. As expected, components accounting for lower variance values are increasingly noisy and are likely to contain mostly noise. To address this, we use dimensionality reduction to reduce each 100-wavelength HSI cube to 3 components, resulting in three 1-channel images. For example, Fig. 5 depicts the three components derived from the PCA and t-SNE decompositions for the liver.

2.3.2. Step II: detection of the ablation area

Object detection is a fundamental task in computer vision, which involves identifying the presence and location of objects in an image or video. Over the past decade, deep learning has revolutionized the field of computer vision, where Faster R–CNN (Region-based Convolutional Neural Network) has become one of the most popular deep learning-based approaches for object detection. Faster R–CNN was proposed by Shaoqing Ren et al. [30] and builds upon the success of previous deep learning-based approaches, such as R–CNN and Fast R–CNN. The key innovation of Faster R–CNN is the introduction of a Region Proposal Network (RPN) that generates object proposals in a single forward pass. This is a departure from previous methods that relied on external proposals, such as the selective search algorithm. The RPN uses a fully convolutional neural network to predict object proposals at different scales and aspect ratios. These proposals are then refined by a region-based convolutional network, which predicts the class and location of objects within the proposals. Notably, the RPN shares convolutional layers with the detection network, making it computationally efficient. The entire network is trained end-to-end using a multi-task loss that combines object classification and bounding box regression.

Although several advanced object detection algorithms have been developed since the introduction of Faster R–CNN, including YOLO (You Only Look Once) [31], SSD (Single Shot Detector) [32] and RetinaNet
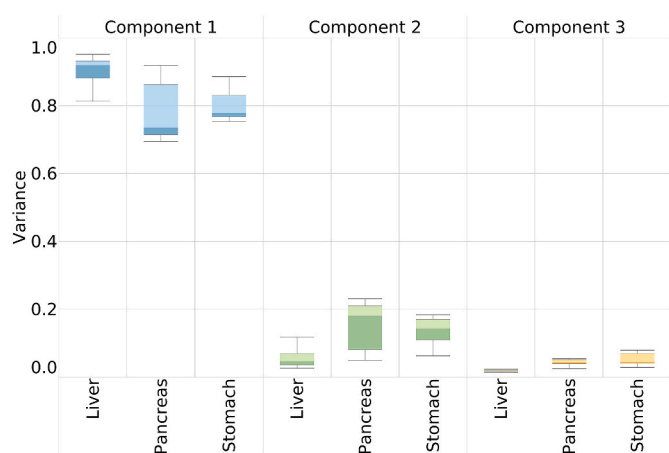
[33], Faster R–CNN has several advantages. It is more accurate than YOLO and SSD because it uses a two-stage detection process that generates region proposals before performing object detection. Additionally, Faster R–CNN is more computationally efficient than RetinaNet because it shares convolutional layers between the region proposal network and the detection network.

Therefore, we selected Faster R–CNN for the detection of ablation areas on hyperspectral images, specifically after dimensional reduction. By training a deep learning model with Faster R–CNN, we identify and locate ablation areas within hyperspectral images. The RPN generates proposals for potential ablation areas, which are then refined by the R–CNN to accurately identify the location and extent of the ablation. This application is particularly useful in the context of laser-mediated thermal treatment, where precise and localized removal of cancer cells is critical for effective patient treatment.

As described in *Step I: dimensionality reduction*, the dataset, comprising 233 hyperspectral cubes with 100 wavelengths each, was converted into 699 single-channel images using PCA and t-SNE decompositions. These images were then divided into training and test subsets and used in the neural network analysis.

We would like to note that we conducted four experiments, each training a different network as shown in Table 1. To investigate the effects of dimensionality reduction and data modality on neural network accuracy, we created four datasets with different combinations of dimensionality reduction types and data modalities. To ensure that network performance estimates are consistent across experiments, we split the dataset identically for all four. Furthermore, we would like to point out that the dataset we obtained is slightly imbalanced, with 40 % of liver images, 32 % of pancreas images, and 28 % of stomach images.

To tackle the multi-task nature of object detection, our network employs two losses: a classification loss $L(y, \widehat{y})_{cls}$ for label prediction (Eq. (1)), and a regression loss $L(y, \widehat{y})_{reg}$ for bounding box prediction (Eq. (2)). We compute the total loss $L(y, \widehat{y})$ as a weighted sum of the two losses (Eq. (3)):

$$L(y, \widehat{y})_{cls} = -\sum y_i * \log(\widehat{y}_i) \tag{1}$$

$$L(y, \widehat{y})_{reg} = |y - \widehat{y}| \tag{2}$$

$$L(y, \widehat{y}) = w_{cls} * L(y, \widehat{y})_{cls} + w_{reg} * L(y, \widehat{y})_{reg} \tag{3}$$

where y is the true class label for $L(y, \widehat{y})_{cls}$ and the target value for $L(y, \widehat{y})_{reg}$, while $\widehat{y}$ is the predicted class probability for $L(y, \widehat{y})_{cls}$ and the predicted target value for $L(y, \widehat{y})_{reg}$. The scalar weights w_{cls} and w_{reg} determine the relative importance of the two losses in multi-task learning. In our study, we set both weights to 1.

During the training phase of our study, we employed the stochastic gradient descent optimizer with specific parameter settings to enhance the effectiveness of the learning process. These settings included an initial learning rate of 0.0025, a momentum of 0.9, and a weight decay of 0.0001. In addition, we implemented a strategy to dynamically adjust the learning rate of the backbone by reducing it by a factor of 10. To avoid unstable gradients during training, we incorporated gradient clipping. It is important to note that all models underwent training for a fixed duration of 100 epochs.

To increase the size of our dataset and prevent overfitting during model training, we used a series of augmentation transformations that were applied during training. These transformations included:

- Contrast limited adaptive histogram equalization (with a probability of 20 %).
- Random-sized crop (with a probability of 20 % and a weight-to-height ratio of 1; the range of crop was randomly selected between $0.7 \times I_h$ and $0.9 \times I_h$, where I_h is the source image height).

Fig. 4. Distribution of the variance explained by the PCA across the different components and organs.
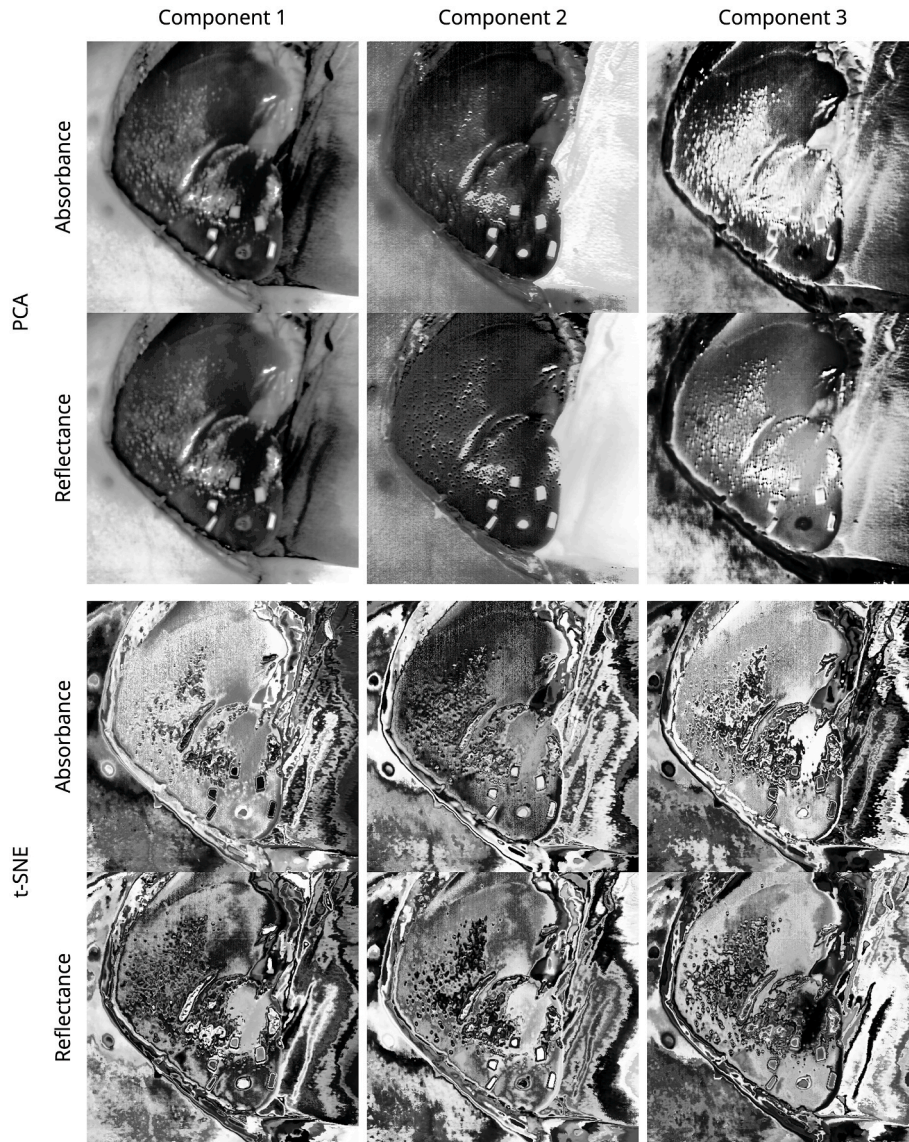
Fig. 5. Example of 3 components obtained by PCA and t-SNE decompositions for the 100-wavelength HSI liver cube for both the absorbance and reflectance modalities.

Table 1

Distribution of the data over the experiments.

ID	Reduction	Modality	Train images	Test images	Total images
1	PCA	Absorbance	558	141	699
2	PCA	Reflectance	558	141	699
3	t-SNE	Absorbance	558	141	699
4	t-SNE	Reflectance	558	141	699

- Rotation (with a probability of 50 % and a random angle between −15° and +15°).
- Horizontal flip (with a probability of 50 %).
- Random brightness and contrast adjustment (with a probability of 20 % and a factor range of −0.2 to +0.2 for both).

We maintained consistency among the trained models by assigning a batch size of 16, which we experimentally determined to allow the GPU to utilize approximately 90–100 % of its memory. The models were trained on a desktop computer equipped with an Intel Core i9-10940X processor clocked at 3.30 GHz, an NVIDIA GeForce RTX 3090 graphics card with 24 GB of video memory, 256 GB of RAM, and the Windows 10 operating system.

2.3.3. Step III: segmentation of the ablation area

As mentioned earlier, the final step in our proposed workflow involves adapting unsupervised segmentation techniques. After considering several options, we finally chose Mean Shift Clustering as our primary method. This non-parametric clustering algorithm has been widely used in many unsupervised segmentation tasks and offers numerous advantages over other algorithms such as k-means and hierarchical clustering. First, unlike k-means, mean shift clustering does not require a predetermined number of clusters, which is often limiting [34]. Second, it is robust to noise and outliers because it assigns data points to the nearest mode of the density function. Finally, it is computationally efficient and does not require pairwise distance computations, unlike hierarchical clustering.

Mean Shift has also been successfully applied in various domains such as computer vision, biology, remote sensing, and others. For example, it has been used for tasks such as histological image segmentation [35] and retinal blood vessel segmentation [36]. Similarly, it has been used to identify subpopulations in single-cell gene expression data [37]. In remote sensing, Mean Shift has been used for forest

segmentation [38]. In our study, we use Mean Shift clustering to segment image data and compare its performance with other clustering algorithms.

We chose Mean Shift Clustering as our method of choice due to its simplicity, effectiveness, and flexibility. This clustering algorithm offers several advantages over traditional methods that rely on predefined assumptions or distance metrics. Mean Shift clustering is nonparametric and relies on density estimation. It identifies the modes or peaks of the density function and assigns data points to the closest mode. The nonparametric nature of Mean Shift clustering makes it particularly suitable for handling complex and irregularly shaped data sets, as it does not assume any specific cluster shape or size. This is a significant advantage when dealing with data that may not conform to traditional clustering assumptions.

Another valuable feature of Mean Shift clustering is its ability to automatically determine the optimal number of clusters. Traditional clustering methods often struggle with determining the appropriate number of clusters, which can be a challenging task. In the case of hyperspectral data applications, such as our specific use case involving laser-induced damage to tissue, the number of clusters representing different classes of damage is unknown in advance. Laser-induced damage to tissue exhibits heterogeneity and is typically classified based on its effect on cells [6]. Fig. 2 provides visual examples where different classes of damage, such as the central area, the ring area, and the outer undamaged area, can be easily distinguished. However, the number of clusters representing these classes of thermal damage in HSI data is not known a priori. Therefore, Mean Shift clustering is an appropriate choice for this application.

3. Results

After training the networks on the dataset described in *Step II: Detection of the ablation area* and detailed in Table 1, we observed a consistent trend in the dynamics of the mean Average Precision (mAP) values. However, it is important to highlight that there were significant variations in the values obtained among the networks we trained. In particular, the highest mAP value of 0.744 was obtained by the model trained on the PCA + Reflectance dataset. Conversely, the model trained on the PCA + Absorbance dataset yielded the best mAP value of 0.712. The t-SNE-based models yielded mAP values of 0.726 for the t-SNE + Absorbance dataset and 0.695 for the t-SNE + Reflectance dataset. A visual representation of the mAP changes during the training process is shown in Fig. 6, which illustrates these fluctuations. It is also important to note that these evaluations were performed on an unseen test subset of 141 images.

After training and testing the ablation detection networks, we proceeded to evaluate the performance of the segmentation component
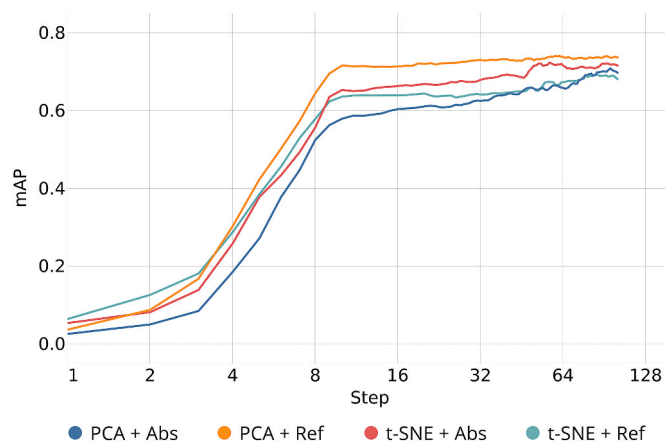

Fig. 6. The changes of mAP over training, calculated on the test subset.

within the proposed workflow. To accomplish this, we compared the selected clustering algorithm, Mean Shift, with several modern and state-of-the-art unsupervised solutions. These solutions included k-means, BIRCH, agglomerative clustering, spectral clustering, Gaussian Mixture Models (GMM), affinity propagation, DBSCAN (Density-Based Spatial Clustering of Applications with Noise), and OPTICS (Ordering Points To Identify the Clustering Structure). A visual comparison of these algorithms is presented in Fig. 7.

Based on the results obtained, it is evident that the nature of the ablation segmentation results differs significantly from one algorithm to another. An interesting observation is that the two most accurate clustering solutions, namely DBSCAN and OPTICS, which are known for their reliability against noise and outliers, had difficulties in performing normal segmentation. Despite the fact that both algorithms do not require a predefined number of clusters and automatically determine the number of clusters based on the density and connectivity of the data points, they showed a tendency to oversegment the image, creating unnecessary small regions. Similar to DBSCAN and OPTICS, the affinity propagation clustering algorithm also showed a tendency to oversegment hyperspectral images. While DBSCAN and OPTICS are powerful techniques, they have limitations. These limitations include sensitivity to parameter settings, oversegmentation in complex scenes, low resilience to image artifacts such as noise, texture, and uneven illumination, and difficulty in handling objects with similar intensities or textures. In our study, we confirm these limitations and demonstrate the inability of the affinity propagation clustering algorithm, DBSCAN and OPTICS to be effectively applied to the collected hyperspectral images.

On the contrary, K-means, BIRCH, agglomerative clustering, spectral clustering, and GMM demonstrate superior performance in segmentation compared to affinity propagation, DBSCAN, and OPTICS. However, a common problem with these algorithms is the inability to automatically determine the optimal number of clusters, requiring manual input from the user. This limitation is particularly significant when analyzing hyperspectral images with multiple wavelengths, as the number of clusters is unknown beforehand.

Considering the obtained results, we have concluded that despite being a relatively older clustering algorithm, Mean Shift offers high-quality segmentation of tissues in hyperspectral images. It also exhibits lower sensitivity to internal parameters and eliminates the need for manual predefinition of the number of clusters.

In addition, our findings highlight a notable disparity between human perception, which relies on three primary colors (red, green, and blue) to perceive a wide range of colors, and 100-channel hyperspectral cameras, which capture a broader range of wavelengths. HSI has shown promise in providing a higher level of information compared to what is visible to the human eye, making it valuable in surgical procedures where the surgeon's vision may be limited.

However, due to the specific nature of hyperspectral data, a significant challenge arises due to the lack of reference numbers for laser-induced classes of damage in the images. This limitation hinders our evaluation of experimental laser cancer therapy and prevents accurate analysis of tissue treatment progress during therapy [6]. Accurate classification of different types of laser-induced damage is critical for understanding the effectiveness of therapy. Without a reliable reference system, tracking changes in tissue condition over time and drawing meaningful conclusions from the data becomes challenging.

To address this issue, we used this tailored workflow for laser-induced damage classes in HSI images. This workflow enables more accurate evaluation of tissue treatment progress in experimental laser cancer therapy studies, enhancing our ability to assess the effectiveness of laser treatment and improve the analysis of tissue response to therapy.

After processing the entire dataset utilizing the trained Faster R–CNN neural network for ablation detection and the unsupervised Mean Shift clustering algorithm for ablation segmentation, we obtained the results shown in Fig. 8. In this plot, we did not aggregate by tissue temperature or organ; instead, we estimated how the number of clusters varies for the
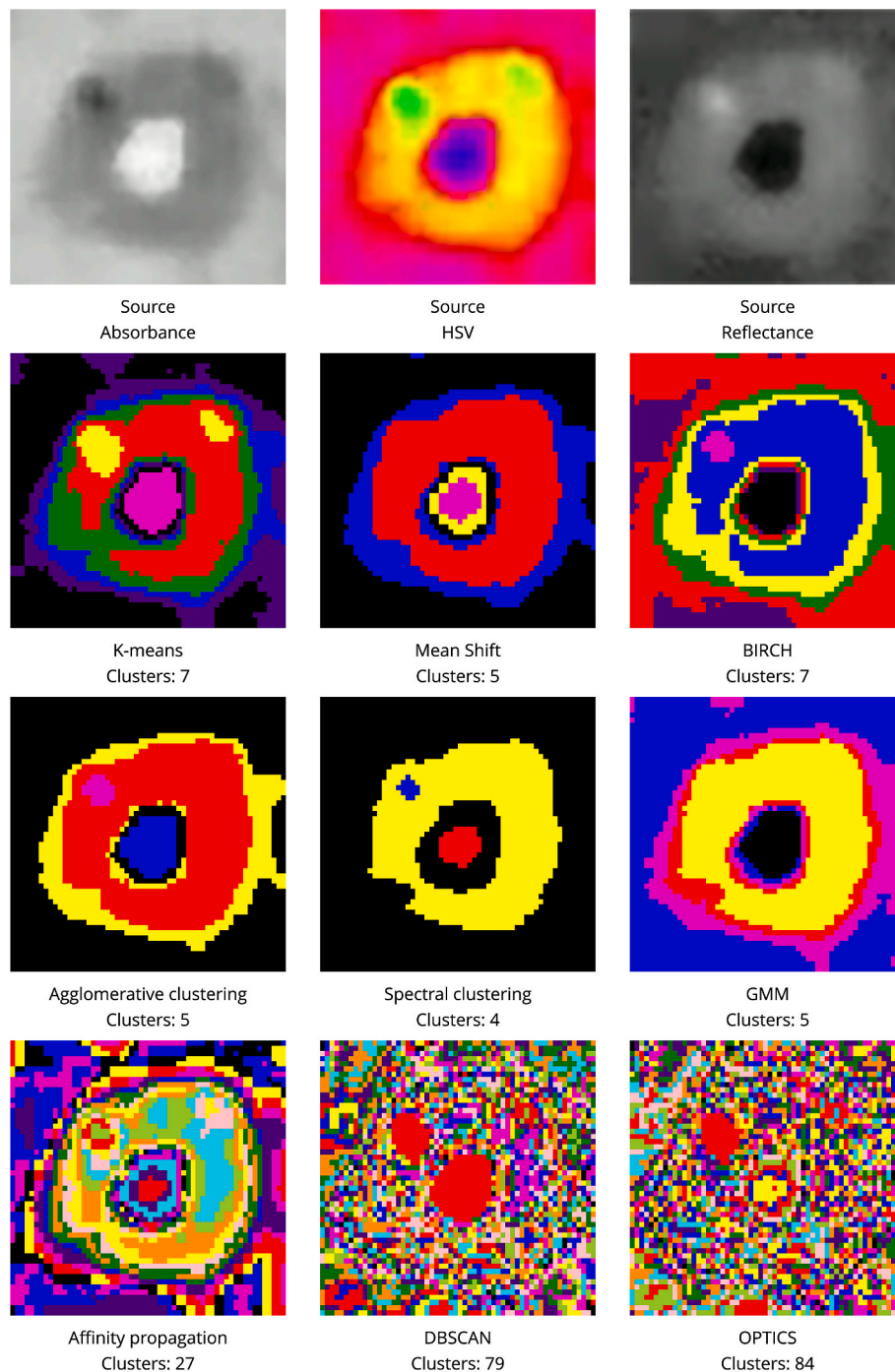
Fig. 7. Comparison of ablation segmentation performed with different unsupervised algorithms. The top row represents the input data for clustering algorithms.

studied modalities, namely absorbance and reflectance.

As depicted, the number of clusters exhibits significant fluctuations in the reflectance modality. It initially increases and reaches a peak from 550 to 600 nm, achieving nearly 6 clusters for the ablation zone. Subsequently, the number of clusters dramatically drops to 4 within the range of 650–700 nm, and then gradually increases again to approximately 5 clusters at 900 nm. On average, the number of clusters for the reflectance modality was 4.5 ± 1.7.

In contrast, the number of clusters in the absorbance modality exhibits less oscillation and remains relatively stable over the entire wavelength range. It increases from 2 to 3 clusters for the first 50 wavelengths, i.e. from 500 to 550 nm. After 550 nm, the number of clusters stabilizes, with a slight change to 4 clusters for the ablation zone

within the wavelength range of 800 nm–850 nm. The average number of clusters for the absorbance modality is 3.6 ± 1.4, which is closer to human vision than the average number of clusters for reflectance. This finding is supported by our previous research [6], where experienced surgeons manually graded the following classes of damage as 3.

Upon independent analysis of each organ, as presented in Table 2 and Fig. 9, a consistent pattern emerges in the changing number of clusters across different organs, as described previously. In particular, the number of clusters for the pancreas demonstrates a close alignment in both the absorbance and reflectance datasets, with a distinct difference observed in the range of 500–625 nm. Subsequently, a strong alignment is observed from 625 to 800 nm, while a slight variation in the number of clusters becomes apparent beyond 800 nm, indicating a
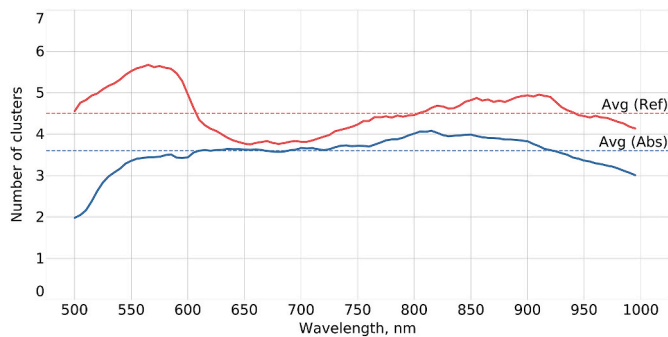
Fig. 8. Cluster number comparison between absorbance (blue) and reflectance (red) modalities.

Table 2
Number of clusters across studied organs.

Organ	Absorbance	Reflectance
Liver	3.6 ± 1.4	4.8 ± 1.9
Pancreas	3.4 ± 1.2	3.9 ± 1.4
Stomach	3.6 ± 1.3	4.5 ± 1.5
Overall	**3.6 ± 1.4**	**4.5 ± 1.7**

downward trend.

Regarding the dynamics of the liver and stomach subsets, we observe similar changes in cluster numbers on absorbance for both organs. The cluster number starts to increase from 2 clusters within the range of 500–600 nm. Subsequently, the cluster number remains relatively stable, with minor oscillations around the average value of 3.6 for both the liver and stomach. In contrast, the cluster number exhibits more fluctuations in the reflectance subset and shows an M-shaped pattern. There are two peaks within the range of 500–600 nm and 800–950 nm, with a cavity observed within the wavelength range of 625 nm–725 nm. It is worth noting that the cluster number for the stomach fluctuates less on the reflectance subset compared to other organs, typically ranging between 4 and 5 clusters.

In addition, we provide the cluster number variation plots as a function of temperature thresholds for the entire dataset (see Fig. S1) and three subsets (liver, pancreas, and stomach; see Figs. S2–S4) in *Supplementary Information*. The cluster number variation plots represent changes in the number of distinct clusters identified at different temperature thresholds for the respective subsets.

4. Discussion

The presented results provide valuable insights into the performance of different algorithms and modalities in the context of ablation detection and segmentation in HSI acquired during laser treatment intended for localized tumor removal. A major objective of this study was to investigate the data processing approaches which allow the extraction of valuable information and segmentation of the hyperspectral images.

4.1. Dimensionality reduction

In the context of dimensionality reduction, it is important to understand the strengths and weaknesses of both PCA and t-SNE and to choose the appropriate method based on the specific research question or goal. While PCA is a widely used linear technique that can effectively capture the dominant variations in the data, t-SNE provides nonlinear dimensionality reduction and can reveal intricate structures and relationships within the data.

To enhance the dimensionality reduction process, it is advisable to incorporate other complementary methods or techniques. For example,

kernel PCA or local linear embedding can be employed to perform nonlinear dimensionality reduction when the data exhibits complex nonlinear relationships. Spectral unmixing or segmentation techniques can also be applied to extract spectral features or identify regions of interest in HSI data.

In addition to the dimensionality reduction techniques employed, there are a number of algorithms that can be beneficial for similar multi-step workflows for processing hyperspectral data. These algorithms are employed for the selection of hyperspectral bands aimed at eliminating spectral redundancy and reducing computational costs [39–41]. The challenge with band selection lies in choosing a set of representative bands that can achieve better or, at the very least, comparable performance to using the original bands in specific applications such as classification, detection, or spectral unmixing. However, these algorithms differ from those utilized in our study by their nature. In the proposed workflow, we employed a processing block that linearly or non-linearly transforms 100 hyperspectral bands into three one-channel components (images). This number of components, on average, explains 98.3 % of the data variance, which, according to our assumption, is sufficient for subsequent use in the detection or segmentation stage. Furthermore, three-channel images align well with the input requirements of most neural networks, allowing the use of pre-trained backbones and model weights from sources such as ImageNet or COCO. In contrast, band selection does not guarantee that the selected three bands will explain the same or a higher level of variance. Typically, scientists and researchers employ more than 10 bands for testing their algorithms and models [42]. A key challenge associated with workflows employing the band selection approach is that subsequent blocks, such as detection or segmentation networks, must appropriately process images of dimensions $X \times Y \times N$, where N is the number of selected bands or components. If $N > 3$, it necessitates a change in the architecture of the network, which is usually beyond the scope of a study. Nevertheless, we have come to the point where the use of transformation-based approaches (PCA, t-SNE, UMAP) is more beneficial than band selection, especially in the early stages of workflow development. These algorithms allow for a similar level of explainability (redundancy) with a lower number of linear or non-linear components. Expanding on this understanding and exploring the advantages of transformation-based approaches over band selection could provide valuable insights for researchers and practitioners in the field.

In our study, we integrated both PCA and t-SNE into the processing workflow to leverage their respective advantages and compare their applicability to the specific dataset. By combining these methods, we aimed to capture both the dominant variations through linear PCA and the intricate structures through nonlinear t-SNE. This integration allowed us to gain a comprehensive understanding of the data and improve the analysis of the tissue treatment progress in the evaluation of laser-induced effects. Overall, the integration of PCA and t-SNE, along with other complementary techniques, can provide a more robust and insightful analysis of hyperspectral data, enabling researchers to effectively extract meaningful information and make accurate interpretations.

4.2. Detection of the ablation area

Object detection neural networks, especially Faster R–CNN, play a crucial role in HSI, particularly in tasks such as identifying and localizing ablation areas during medical procedures. The unique two-stage detection process of Faster R–CNN, which includes region proposal generation and subsequent object detection, significantly improves accuracy and computational efficiency compared to other methods. In particular, the use of shared convolutional layers between the region proposal network and the detection network further enhances computational efficiency and differentiates it from one-stage approaches such as YOLO (You Only Look Once) and SSD (Single Shot Detector). This unique feature positions Faster R–CNN as a valuable tool in HSI
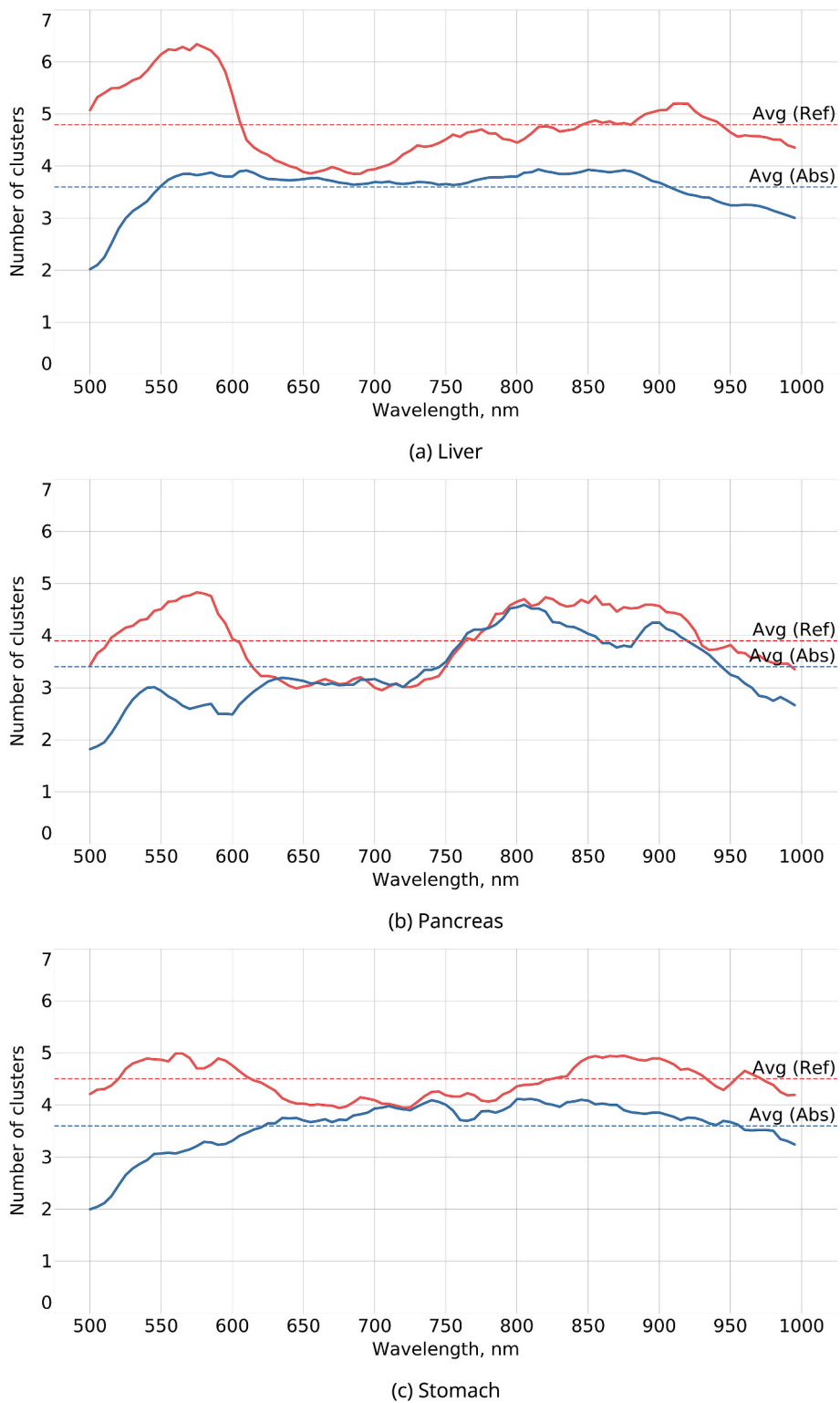
(a) Liver

(b) Pancreas

(c) Stomach

Fig. 9. Cluster number comparison across wavelengths for the studied organs.

applications, providing superior accuracy and computational efficiency compared to alternative algorithms such as RetinaNet.

Our study revealed a consistent trend in the dynamics of mAP values during training (Fig. 6), with notable variations across different datasets. The highest mAP, 0.744, was achieved by the model trained on the PCA + Reflectance dataset, demonstrating the importance of dimensionality reduction and reflectance data. The PCA + Absorbance model yielded a close mAP value of 0.712, indicating the effectiveness of the absorbance

data combined with PCA. The t-SNE-based models also performed well, with mAP values of 0.726 for t-SNE + Absorbance and 0.695 for t-SNE + Reflectance. These evaluations were performed on an unseen test subset of 141 images, confirming the models' ability to generalize. The combination of Faster R–CNN and various dimensionality reduction and data modality pairs effectively detected, localized, and classified objects within hyperspectral images.

The observed superior performance of PCA + Reflectance data in

achieving the highest mAP value can be attributed to their complementary characteristics in the experimental setup. PCA reduces the dimensionality of hyperspectral data and improves the efficiency of subsequent processing steps by highlighting essential spectral features. Reflectance data provides insight into the surface properties of objects, aiding discrimination between materials or objects. The synergy between PCA and reflectance likely contributes to the combination's success. PCA focuses on relevant spectral features, while reflectance provides valuable surface information, leading to improved model efficiency and performance. This collaborative benefit is crucial for achieving the highest mAP value. Further analysis could delve into specific spectral bands or principal components that play a substantial role in this success, offering deeper insights into the observed experimental results. This integrated approach not only refines hyperspectral object detection but also contributes to advancements in various fields.

4.3. Segmentation of the ablation area

Various clustering algorithms were assessed for ablation segmentation in HSI. DBSCAN, OPTICS, and affinity propagation resulted in oversegmentation, whereas k-means, BIRCH, agglomerative clustering, spectral clustering, and GMM demonstrated superior performance. However, the latter algorithms necessitate manual input for the number of clusters. In contrast, Mean Shift exhibited high-quality segmentation, diminished sensitivity to parameters, and eliminated the need for manual cluster definition. The adaptability, autonomous cluster center determination, robustness to noise, parameter insensitivity, effective handling of irregular cluster shapes, and limited dependence on initialization make Mean Shift particularly well-suited for the segmentation stage in the proposed workflow. These attributes collectively contribute to its excellence, especially in navigating the dynamic and intricate spectral landscapes of hyperspectral ablation images.

The number of clusters showed significant variation in the reflectance modality, peaking at 550–600 nm and decreasing at 650–700 nm. Conversely, the number of clusters remained stable in the absorbance modality, with a slight change observed at 800–850 nm. On average, there were 4.5 ± 1.7 clusters for reflectance and 3.6 ± 1.4 clusters for absorbance, which aligns more closely with human vision. This observation suggests that the information content regarding the damage classes varies depending on the spectral range, particularly in the case of reflectance. Consequently, limiting the analysis to a specific range may risk losing important information. To further investigate this point, it is recommended to verify whether these clusters correspond to different image regions. Moreover, the use of reflectance enables access to additional information compared to human vision and the absorbance case.

Consistent patterns emerged across different organs, with the pancreas showing alignment in both modalities. The liver and stomach subsets exhibited similar changes in cluster numbers in absorbance, while the reflectance subset showed more fluctuations. Detailed cluster number variation plots for temperature thresholds are provided in *Section 1 of Supplementary Information.*

The variation in the number of clusters under different organs or temperature thresholds in hyperspectral ablation segmentation is influenced by several factors that are critical for tailoring segmentation approaches to specific organs, temperature conditions, and stages of laser ablation. Understanding and accounting for these factors is essential and ultimately contributes to accurate and meaningful analysis of tissue treatment progress. These factors are as follows:

1. **Tissue-specific Spectral Characteristics.** Different organs exhibit unique spectral characteristics, influenced by their composition, structure, and biological properties. The inherent diversity in tissue types leads to variations in the number of clusters required to adequately represent the spectral information associated with ablation-induced changes. For instance, the pancreas, liver, and stomach may have distinct spectral responses to laser-induced

thermal treatment, necessitating varying numbers of clusters for accurate segmentation.

2. **Temperature-dependent Spectral Variations.** The hyperspectral images capture temperature-induced changes in tissues during laser ablation. As the temperature thresholds increase, the spectral signatures of tissues may evolve, leading to variations in the required number of clusters.

3. **Spatial and Temporal Dynamics.** Organs may exhibit spatial and temporal variations in their responses to laser treatment. The number of clusters could vary spatially within an organ, reflecting localized variations in tissue damage. Additionally, different temperature thresholds may correspond to distinct temporal stages of the ablation process, introducing variability in the spectral patterns and, consequently, the optimal number of clusters.

4. **Complexity of Hyperspectral Data.** HSI generates rich and complex datasets with detailed spectral information at multiple wavelengths. The diversity in tissue responses, coupled with the intricate nature of hyperspectral data, contributes to the variation in the number of clusters required for effective segmentation across different organs and temperature thresholds.

4.4. Limitations and future directions

As we continue to refine our approach, it is imperative to consider various factors that may influence the reliability and generalizability of our findings. With this in mind, we highlight key areas for improvement and outline our strategies for future development:

1. **Data Collection.** Given the unique nature of experimental studies involving animals, our study was confined to a limited sample size of three pigs. However, our future endeavors will prioritize the collection of additional heterogeneous datasets to enhance the robustness and generalizability of our findings.

2. **Data Annotation.** The presence of only one expert annotator in our study precluded the assessment of inter-annotator agreement, thereby limiting our ability to assess labeling quality. In future research, involving multiple annotators will be essential to identify and correct biases, resulting in more neutral and balanced labels and ultimately enhancing overall data quality.

3. **RGB vs HSI.** In exploring the potential value of contrasting detection performance between models trained on hyperspectral images and those trained on original RGB images, it is evident that such a comparison could provide crucial insights into the distinct advantages of hyperspectral imaging in medical contexts. Whereas RGB images offer visual data limited to three color channels, hyperspectral images provide a significantly richer spectral signature spanning hundreds of contiguous bands. This expanded spectral range enables superior discrimination between diverse tissues or materials. By contrasting the performance of models trained on dimensionally reduced hyperspectral data with those trained on RGB images, we can highlight the enhanced discriminative power and diagnostic potential inherent in hyperspectral imaging. Such a comparative analysis would underscore the importance of exploiting the complementary spectral information provided by hyperspectral data in medical tasks. Therefore, our forthcoming study will encompass a comprehensive experimental comparison between regular and hyperspectral images, further enriching our understanding of their respective capabilities and implications for medical imaging methodologies.

4. **Model Comparison.** Currently, expanding the number of stages or integrating additional data modalities, algorithms, or models would necessitate a considerable increase in the number of experiments conducted. In forthcoming studies, we intend to constrain certain degrees of freedom, such as data modality, and delve deeper into exploring dimensionality reduction algorithms or object detection models. This strategic approach aims to foster a comprehensive and

in-depth understanding of these components, thereby enriching our analyses and insights.

5. Conclusion

This study introduces a comprehensive multistage workflow for analyzing ablation detection and segmentation in hyperspectral images obtained during experimental laser treatment on *in-vivo* liver, pancreas, and stomach tissues. Leveraging the combined strengths of PCA and t-SNE, our approach enhances hyperspectral data analysis, providing valuable insights into tissue disease progression during laser-mediated cancer treatment.

The application of Faster R–CNN for ablation detection underscores the superiority of this deep learning-based algorithm in accurately identifying and localizing ablation areas within hyperspectral images. Evaluation on an independent test set reaffirms the generalization capability of the trained models, indicating their potential applicability in real-world scenarios. The choice of dimensionality reduction technique and data modality significantly influences object detection performance.

In the realm of ablation area segmentation, the Mean Shift algorithm emerges as a standout performer, offering high-quality segmentation without the need for manual cluster definition. This automated and reliable approach contributes to efficient hyperspectral image segmentation.

Our research opens avenues for future exploration, including further refinement of algorithmic approaches, exploration of novel dimensionality reduction, object detection and segmentation techniques, and extension of applications to a broader range of medical imaging scenarios. Investigating the impact of HSI on different cancer types and treatment modalities can provide valuable insights for personalized therapeutic interventions. By judiciously selecting HSI processing techniques and data modalities, researchers and medical professionals can extract meaningful information from hyperspectral data, fostering improved analysis, interpretation, and decision-making in laser cancer therapy and other medical applications.

Data availability

The data supporting the key findings of this study are presented within the article and its supplementary information files. All essential components of the study, including curated source code, data, and trained models, have been made publicly available:

- **Source code:** https://github.com/ViacheslavDanilov/hsi_analysis.
- **Dataset:** https://doi.org/10.5281/zenodo.10444212.
- **Models:** https://doi.org/10.5281/zenodo.10444269.

CRediT authorship contribution statement

Viacheslav V. Danilov: Writing – review & editing, Writing – original draft, Visualization, Validation, Software, Methodology, Formal analysis, Data curation, Conceptualization. **Martina De Landro:** Writing – original draft, Investigation, Supervision, Data curation, Conceptualization. **Eric Felli:** Writing – review & editing, Resources, Investigation. **Manuel Barberio:** Writing – review & editing, Resources, Investigation. **Michele Diana:** Writing – review & editing, Resources. **Paola Saccomandi:** Writing – review & editing, Writing – original draft, Investigation, Supervision, Project administration, Funding acquisition, Data curation, Conceptualization.

Declaration of competing interest

The authors declare that they have no known competing financial interests or personal relationships that could have appeared to influence the work reported in this paper.

Appendix A. Supplementary data

Supplementary data to this article can be found online at https://doi.org/10.1016/j.compbiomed.2024.108849.

References

[1] L. Crocetti, T. de Baére, P.L. Pereira, F.P. Tarantino, CIRSE standards of practice on thermal ablation of liver tumours, Cardiovasc. Intervent. Radiol. 43 (2020) 951–962, https://doi.org/10.1007/S00270-020-02471-Z/METRICS.

[2] R. Geoghegan, G. ter Haar, K. Nightingale, L. Marks, S. Natarajan, Methods of monitoring thermal ablation of soft tissue tumors – a comprehensive review, Med. Phys. 49 (2022) 769–791, https://doi.org/10.1002/MP.15439.

[3] M. De Landro, C. Giraudeau, J. Verde, K. Ambarki, S. Korganbayev, A. Wolf, H. Odéen, P. Saccomandi, Characterization of susceptibility artifacts in magnetic resonance thermometry images during laser interstitial thermal therapy: dimension analysis and temperature error estimation, Phys. Med. Biol. 68 (2023) 085022, https://doi.org/10.1088/1361-6560/ACBC62.

[4] S. Korganbayev, A. Orrico, L. Bianchi, D. Paloschi, A. Wolf, A. Dostovalov, P. Saccomandi, PID controlling approach based on FBG array measurements for laser ablation of pancreatic tissues, IEEE Trans. Instrum. Meas. 70 (2021), https://doi.org/10.1109/TIM.2021.3112790.

[5] D.A. Gil, L.M. Swift, H. Asfour, N. Muselimyan, M.A. Mercader, N.A. Sarvazyan, Autofluorescence hyperspectral imaging of radiofrequency ablation lesions in porcine cardiac tissue, J. Biophot. 10 (2017) 1008–1017, https://doi.org/10.1002/JBIO.201600071.

[6] M. De Landro, E. Felli, T. Collins, R. Nkusi, A. Baiocchini, M. Barberio, A. Orrico, M. Pizzicannella, A. Hostettler, M. Diana, P. Saccomandi, Prediction of in vivo laser-induced thermal damage with hyperspectral imaging using deep learning, Sensors 21 (2021) 6934, https://doi.org/10.3390/s21206934.

[7] P. Lanka, K.J. Francis, H. Kruit, A. Farina, R. Cubeddu, S.K.V. Sekar, S. Manohar, A. Pifferi, Optical signatures of radiofrequency ablation in biological tissues, Sci. Rep. 11 (2021), https://doi.org/10.1038/s41598-021-85653-0.

[8] A. Bossi, L. Bianchi, P. Saccomandi, A. Pifferi, Temporal evolution of optical properties at different temperatures of biological tissues, in: S. Fantini, P. Taroni (Eds.), Optical Tomography and Spectroscopy of Tissue XV, SPIE, 2023, p. 41, https://doi.org/10.1117/12.2649110.

[9] M.H. Aref, I.H. Aboughaleb, A.B.M. Youssef, Y.H. El-Sharkawy, Hyperspectral image-based analysis of thermal damage for ex-vivo bovine liver utilizing radiofrequency ablation, Surg. Oncol. 38 (2021) 101564, https://doi.org/10.1016/J.SURONC.2021.101564.

[10] M. De Landro, I.E. García-Molina, M. Barberio, E. Felli, V. Agnus, M. Pizzicannella, M. Diana, E. Zappa, P. Saccomandi, Hyperspectral imagery for assessing laser-induced thermal state change in liver, Sensors 21 (2021) 643, https://doi.org/10.3390/S21020643.

[11] J. Yoon, Hyperspectral imaging for clinical applications, Biochip. J. 16 (2022) 1–12, https://doi.org/10.1007/s13206-021-00041-0.

[12] D. Datta, P.K. Mallick, A.K. Bhoi, M.F. Ijaz, J. Shafi, J. Choi, Hyperspectral image classification: potentials, challenges, and future directions, Comput. Intell. Neurosci. 2022 (2022), https://doi.org/10.1155/2022/3854635.

[13] J.D. Pallua, A. Brunner, B. Zelger, C.W. Huck, M. Schirmer, J. Laimer, D. Putzer, M. Thaler, B. Zelger, New perspectives of hyperspectral imaging for clinical research, NIR News 32 (2021) 5–13, https://doi.org/10.1177/09603360211024971.

[14] G. Lu, B. Fei, Medical hyperspectral imaging: a review, J. Biomed. Opt. 19 (2014) 010901, https://doi.org/10.1117/1.JBO.19.1.010901.

[15] H. Gao, M. Wang, X. Sun, X. Cao, C. Li, Q. Liu, P. Xu, Unsupervised dimensionality reduction of medical hyperspectral imagery in tensor space, Comput. Methods Progr. Biomed. 240 (2023) 107724, https://doi.org/10.1016/J.CMPB.2023.107724.

[16] H. Li, J. Cui, X. Zhang, Y. Han, L. Cao, Dimensionality reduction and classification of hyperspectral remote sensing image feature extraction, Rem. Sens. 14 (2022) 4579, https://doi.org/10.3390/RS14184579.

[17] R. Cui, H. Yu, T. Xu, X. Xing, X. Cao, K. Yan, J. Chen, Deep learning in medical hyperspectral images: a review, Sensors 22 (2022) 9790, https://doi.org/10.3390/S22249790, 2022.

[18] J.M. Murphy, M. Maggioni, Unsupervised clustering and active learning of hyperspectral images with nonlinear diffusion, IEEE Trans. Geosci. Rem. Sens. 57 (2017) 1829–1845, https://doi.org/10.1109/TGRS.2018.2869723.

[19] S.L. Polk, K. Cui, A.H.Y. Chan, D.A. Coomes, R.J. Plemmons, J.M. Murphy, Unsupervised diffusion and volume maximization-based clustering of hyperspectral images, Rem. Sens. 15 (2023) 1053, https://doi.org/10.3390/RS15041053.

[20] B. Fei, Medical Hyperspectral Imaging: Artificial Intelligence and Image-Guided Surgery, (n.d.). https://www.optica.org/events/webinar/2021/01_january/medical_hyperspectral_imaging_artificial_intellige/(accessed January 2, 2024).

[21] A. Kulcke, A. Holmer, P. Wahl, F. Siemers, T. Wild, G. Daeschlein, A compact hyperspectral camera for measurement of perfusion parameters in medicine, Biomed. Eng. 63 (2018) 547–556, https://doi.org/10.1515/bmt-2017-0145.

[22] A. Kulcke, A. Holmer, P. Wahl, F. Siemers, T. Wild, G. Daeschlein, A compact hyperspectral camera for measurement of perfusion parameters in medicine, Biomed. Eng. 63 (2018) 547–556, https://doi.org/10.1515/BMT-2017-0145.

[23] I. Jolliffe, Principal Component Analysis, 2002, https://doi.org/10.1007/b98835.

[24] L. van der Maaten, G. Hinton, Visualizing Data using t-SNE, J. Mach. Learn. Res. 9 (2008) 2579–2605.

[25] E. Pouyet, N. Rohani, A.K. Katsaggelos, O. Cossairt, M. Walton, Innovative data reduction and visualization strategy for hyperspectral imaging datasets using t-SNE approach, Pure Appl. Chem. 90 (2018) 493–506, https://doi.org/10.1515/pac-2017-0907.

[26] B.M. Devassy, S. George, Dimensionality reduction and visualisation of hyperspectral ink data using t-SNE, Forensic Sci. Int. 311 (2020) 110194, https://doi.org/10.1016/j.forsciint.2020.110194.

[27] A. Miao, J. Zhuang, Y. Tang, Y. He, X. Chu, S. Luo, Hyperspectral image-based variety classification of waxy maize seeds by the t-SNE model and procrustes analysis, Sensors 18 (2018) 4391, https://doi.org/10.3390/S18124391, 2018, Vol. 18, Page 4391.

[28] S.P. Mohanty, D.P. Hughes, M. Salathé, Using deep learning for image-based plant disease detection, Front. Plant Sci. 7 (2016) 1419, https://doi.org/10.3389/fpls.2016.01419.

[29] R. Silva, P. Melo-Pinto, t-Sne, A study on reducing the dimensionality of hyperspectral data for the regression problem of estimating oenological parameters, Artif. Intell. Agric. 7 (2023) 58–68, https://doi.org/10.1016/j.aiia.2023.02.003.

[30] S. Ren, K. He, R. Girshick, J. Sun, Faster R-CNN: towards real-time object detection with region proposal networks, Adv. Neural Inf. Process. Syst. 28 (2015).

[31] J. Redmon, S. Divvala, R. Girshick, A. Farhadi, You only Look once: unified, real-time object detection, 779–788, https://www.cv-foundation.org/openaccess/content_cvpr_2016/html/Redmon_You_Only_Look_CVPR_2016_paper.html, 2016. (Accessed 8 May 2023).

[32] W. Liu, D. Anguelov, D. Erhan, C. Szegedy, S. Reed, C.Y. Fu, A.C. Berg, SSD: single shot multibox detector, lecture notes in computer science (including subseries lecture notes in artificial intelligence and lecture notes in bioinformatics) 9905, LNCS (2016) 21–37, https://doi.org/10.1007/978-3-319-46448-0_2.

[33] T.Y. Lin, P. Goyal, R. Girshick, K. He, P. Dollar, Focal loss for dense object detection. Proceedings of the IEEE International Conference on Computer Vision 2017-October, 2017, pp. 2999–3007, https://doi.org/10.1109/ICCV.2017.324.

[34] D. Comaniciu, P. Meer, Mean shift: a robust approach toward feature space analysis, IEEE Trans. Pattern Anal. Mach. Intell. 24 (2002) 603–619, https://doi.org/10.1109/34.1000236.

[35] G. Wu, X. Zhao, S. Luo, H. Shi, Histological image segmentation using fast mean shift clustering method, Biomed. Eng. Online 14 (2015), https://doi.org/10.1186/S12938-015-0020-X.

[36] J.V.B. Soares, J.J.G. Leandro, R.M. Cesar, H.F. Jelinek, M.J. Cree, Retinal vessel segmentation using the 2-D Gabor wavelet and supervised classification, IEEE Trans. Med. Imag. 25 (2006) 1214–1222, https://doi.org/10.1109/TMI.2006.879967.

[37] X. Qiu, A. Hill, J. Packer, D. Lin, Y.A. Ma, C. Trapnell, Single-cell mRNA quantification and differential analysis with Census, Nat. Methods 14 (2017) 309–315, https://doi.org/10.1038/nmeth.4150, 2017 14:3.

[38] W. Xiao, A. Zaforemska, M. Smigaj, Y. Wang, R. Gaulton, Mean shift segmentation assessment for individual forest tree delineation from airborne lidar data, Rem. Sens. 11 (2019) 1263, https://doi.org/10.3390/RS11111263, 2019, Vol. 11, Page 1263.

[39] P.R. Lorenzo, L. Tulczyjew, M. Marcinkiewicz, J. Nalepa, Hyperspectral band selection using attention-based convolutional neural networks, IEEE Access 8 (2020) 42384–42403, https://doi.org/10.1109/ACCESS.2020.2977454.

[40] C. Zhang, Z. Zhang, D. Yu, Q. Cheng, S. Shan, M. Li, L. Mou, X. Yang, X. Ma, Unsupervised band selection of medical hyperspectral images guided by data gravitation and weak correlation, Comput. Methods Progr. Biomed. 240 (2023) 107721, https://doi.org/10.1016/j.CMPB.2023.107721.

[41] R. Yang, L. Su, X. Zhao, H. Wan, J. Sun, Representative band selection for hyperspectral image classification, J. Vis. Commun. Image Represent. 48 (2017) 396–403, https://doi.org/10.1016/J.JVCIR.2017.02.002.

[42] W. Sun, Q. Du, Hyperspectral band selection: a review, IEEE Geosci. Rem. Sens. Mag. 7 (2019) 118–139, https://doi.org/10.1109/MGRS.2019.2911100.